Article

TRANSPARENT PROCESS

EMBO reports

OCRL regulates lysosome positioning and mTORC1 activity through SSX2IP-mediated microtubule anchoring

Biao Wang[1], Wei He[1], Philipp P Prosseda[1], Liang Li[1], Tia J Kowal[1], Jorge A Alvarado[1], Qing Wang[1], Yang Hu[1] & Yang Sun[1,2,*]

Abstract

Lysosomal positioning and mTOR (mammalian target of rapamycin) signaling coordinate cellular responses to nutrient levels. Inadequate nutrient sensing can result in growth delays, a hallmark of Lowe syndrome. OCRL mutations cause Lowe syndrome, but the role of OCRL in nutrient sensing is unknown. Here, we show that OCRL is localized to the centrosome by its ASH domain and that it recruits microtubule-anchoring factor SSX2IP to the centrosome, which is important in the formation of the microtubule-organizing center. Deficiency of OCRL in human and mouse cells results in loss of microtubule-organizing centers and impaired microtubule-based lysosome movement, which in turn leads to mTORC1 inactivation and abnormal nutrient sensing. Centrosome-targeted PACT-SSX2IP can restore microtubule anchoring and mTOR activity. Importantly, boosting the activity of mTORC1 restores the nutrient sensing ability of Lowe patients' cells. Our findings highlight mTORC1 as a novel therapeutic target for Lowe syndrome.

Keywords lowe syndrome; lysosome positioning; microtubule nucleation; mTOR; OCRL

Subject Categories Cell Adhesion, Polarity & Cytoskeleton; Molecular Biology of Disease; Signal Transduction

DOI 10.15252/embr.202052173 | Received 18 February 2021 | Revised 18 March 2021 | Accepted 8 April 2021 | Published online 13 May 2021

EMBO Reports (2021) 22: e52173

Introduction

Lysosome positioning and motility are tightly linked to mTORC1 activity and nutrient sensing (Korolchuk *et al,* 2011; Lawrence & Zoncu, 2019). In a nutrient-rich environment, lysosomes migrate to the cell periphery, which activates mTORC1 via membrane-bound signaling molecules (Cai *et al,* 2006; Korolchuk *et al,* 2011). In a nutrient-poor environment, lysosomes move to the perinuclear region and cluster at the microtubule-organizing center (MTOC), which inhibits mTOR activity (Matteoni & Kreis, 1987; Korolchuk *et al,* 2011). Defects in lysosomal positioning and mTOR dysfunction contribute to developmental and degenerative neurological diseases (Parenti *et al,* 2015; Sabatini, 2017).

Lowe syndrome is a rare X-linked developmental neurologic disease characterized by eye abnormalities, renal proximal tubular dysfunction, and intellectual and growth retardation (Bokenkamp & Ludwig, 2016). Mutations in *OCRL1,* which encodes an inositol 5-phosphatase that dephosphorylates $PI(4,5)P_2$ to PI4P, cause Lowe syndrome (Zhang *et al,* 1995). OCRL is a multidomain protein with a characteristic phosphatase domain, ASH (ASPM-SPD-2-Hydin) domain, and a RhoGAP-like domain (Erdmann *et al,* 2007). The ASH and RhoGAP-like domains mediate interaction of OCRL with proteins involved in trafficking, including Rab proteins, clathrins, and proteins associated with cytoskeleton, such as Cdc42 and Rac1 (Lowe, 2005; Erdmann *et al,* 2007; Hagemann *et al,* 2012). The ASH domain is also involved in centrosome-related processes (Ponting, 2006; Schou *et al,* 2014). Disease-causing mutations have been shown in the phosphatase domain (Bokenkamp & Ludwig, 2016) and in non-catalytic ASH-RhoGAP domains (Erdmann *et al,* 2007; McCrea *et al,* 2008). However, the underlying mechanisms linking non-catalytic OCRL mutations to Lowe syndrome remain elusive.

Lysosome has been increasingly recognized to play critical roles in degenerative diseases of the brain, eye, and kidneys (Parenti *et al,* 2015; Festa *et al,* 2018). Early studies of Lowe syndrome highlighted autophagosome–lysosome fusion dysfunction and elevated serum lysosomal enzymes in affected patients (Ungewickell & Majerus, 1999; De Leo *et al,* 2016). More recently, lysosome positioning and mTOR signaling defects have been linked to intellectual disability and growth retardation, two major features of Lowe syndrome (Crino, 2011; Parenti *et al,* 2015; Sabatini, 2017). Because developmental delay can occur in patients without renal dysfunction (Abdalla *et al,* 2018), the systemic growth retardation in this disease could be related to an inability to correctly respond to nutrient and growth factor signals. Clinical data show that induction of tubular low molecular weight proteinuria, one of the main kidney dysfunction phenotypes in Lowe syndrome, can occur in patients treated

1 Department of Ophthalmology, Stanford University School of Medicine, Palo Alto, CA, USA
2 Palo Alto Veterans Administration, Palo Alto, CA, USA
*Corresponding author. Tel: +1 650 724 3952; E-mail: yangsun@stanford.edu

with the mTOR inhibitor rapamycin (Fantus *et al,* 2016). Whether mTOR signaling is involved in Lowe syndrome and how lysosome dysfunction contributes to disease pathogenesis remain unclear. In this study, we investigated the role of lysosome positioning and the mTOR pathway in Lowe syndrome.

Results

Persistent perinuclear lysosome positioning in OCRL-deficient cells

We examined lysosome distribution in cells of OCRL-deficient patients (Lowe 1676 and 3265 fibroblasts), and in embryonic fibroblasts (MEFs) prepared from OCRL knockout mice and from a humanized Lowe syndrome mouse model (IOB) (Bothwell *et al,* 2011). LAMP1 immunostaining of control cells (normal human fibroblasts, NHF) and wild type MEFs showed peripheral localization of lysosomes in complete medium and perinuclear localization after 5 h of starvation (Figs 1A–E and EV1A and B). In contrast, OCRL-deficient cells exhibited persistent perinuclear localization in both fed and starved conditions (Figs 1A–E and EV1A and B). This persistent perinuclear lysosome localization in Lowe 1676 cells could be rescued by re-expression wild-type OCRL and the enzymatic deficient OCRL (D499A mutant) also showed a slight rescued effect (Fig EV1C and D), indicating that lysosomal abnormality was caused by OCRL loss. Next, we examined lysosomal biosynthesis by Western blot. We found no significant difference in the LAMP1 protein expression between normal and OCRL-deficient cells (Fig EV1E and F). Subsequently, we analyzed the dynamics of lysosome movement via transfection of a fluorescently labeled lysosome marker (LAMP1-GFP) in live cells. Lysosomes in Lowe 1676 cells were significantly larger than in NHF cells (Fig EV1G and H, Movies EV1 and EV2). To determine lysosome mobility, we used single particle tracking of NHF and Lowe 1676 cells transfected with LAMP1-GFP (Fig 1F). We analyzed lysosome mobility in the peripheral region of these cells; single particle tracking revealed that the lysosomes moved significantly slower in Lowe 1676 cells than in NHF cells (Fig 1G and H). To further confirm the lysosome mobility defects in OCRL knockout and IOB MEFs, we analyzed the formation of lysosome tubulation, which is dependent on lysosome anterograde movement (Li *et al,* 2016). During an 8-h starvation period, lysosome tubulation occurred in the wild-type MEFs, but not in the OCRL-deficient MEFs (Fig 1I and J, Movies EV3–EV5). We therefore concluded that OCRL deficiency prevents anterograde trafficking of lysosomes and consequently leads to a persistent perinuclear lysosome-positioning defect.

mTORC1 inactivation and nutrient sensing abnormality in OCRL-deficient cells

In the presence of nutrients, mTORC1 is recruited and activated at the surface of peripheral lysosomes (Cai *et al,* 2006; Korolchuk *et al,* 2011). Since we observed that numbers of peripheral lysosomes were reduced in OCRL-deficient cells, we hypothesized that mTOR localization might also be affected. In wild-type MEFs, mTOR was localized peripherally in fed conditions and in the perinuclear region in starved conditions (Fig 1B and E). However, OCRL-deficient cells exhibited persistent perinuclear mTOR localization in both fed and starved conditions (Fig 1B and E), indicating that OCRL depletion does not affect the recruitment of mTOR to the lysosomal membrane. mTOR staining of IOB MEFs confirmed this phenotype (Fig EV1A and I). Consistent with these results for mTOR localization, we found that in wild-type cells, serum starvation decreased mTORC1 activity compared with fed conditions, as assayed by the phosphorylation status of mTOR Ser2448 and p70 S6 Kinase (Thr389), whereas in OCRL-deficient cells mTOR activity was consistently lower than in wild-type cells in fed conditions, and also less sensitive to serum starvation (Figs 2A and B, and EV2A and B). Importantly, retina and brain tissues derived from OCRL knockout and Lowe syndrome mice (IOB) also showed decreased mTORC1 activity (Fig EV2C). In addition, we found that reintroducing OCRL in Lowe 1676 cells could significantly restore mTORC1 activity (Fig 2C). We further investigated whether OCRL enzyme activity contributes to the mTOR signaling pathway. However, OCRL inhibitor YU142670 did not affect the phosphorylation status of S6K in NHF cells (Fig EV2D) and reintroducing OCRL-D499A, a mutant with no phosphatase activity, in Lowe 1676 cells partially increased p70 S6 Kinase (Thr389) activity (Fig EV2E and F). These results show that mTORC1 activity is relatively low in OCRL-deficient cells

Figure 1. OCRL deficiency leads to perinuclear lysosome positioning.

A NHF, Lowe 1676, and Lowe 3265 cells were grown in complete media or 5 h serum starvation, then immunostained with LAMP1 antibody. Dashed lines in images outline cell boundaries. Scale bar, 10 μm.

B Wild-type ($Ocrl^{+/y}$) and $Ocrl^{-/-}$ MEF cells were grown in complete media or 5 h serum starvation, then immunostained with indicated antibodies. Dashed lines in images outline cell boundaries. Scale bar, 10 μm.

C Quantitative analyses of lysosome perinuclear distribution in the experiments shown in A. The intracellular distribution of LAMP1-positive vesicles was quantified as described in the Materials and Methods. $n = 3$ per group in which 30 cells were counted per condition per experiment.

D, E Quantitative analyses of lysosome and mTOR perinuclear distribution in the experiments shown in B. The intracellular distribution of mTOR-positive vesicles was quantified as described in the Materials and Methods. $n = 3$ per group in which 30 cells were counted per condition per experiment.

F, G Representative images of the trajectory of GFP signals from NHF ($n = 4$) and Lowe 1676 ($n = 4$) cells transfected with lysosome-GFP. Trajectories were obtained as described (He *et al,* 2016) and labeled in different colors with the same colored circles showing the start of the track. G. Measured MSD ($\langle \Delta r2\ (t) \rangle$) as a function of delay time t for the mobile lysosome trajectories taken at F.

H Diffusion coefficient of lysosome in the experiments shown in G. Means ± SEM of $n = 4$ cells per group.

I Snap images of WT ($Ocrl^{+/y}$), OCRL knockout ($Ocrl^{-/-}$), and IOB MEFs transfected with lysosome-GFP. After transfection, WT, OCRL knockout, and IOB MEFs were left in serum starvation for 8 h. Scale bar, 5 μm.

J Quantitative analyses of tubulated lysosomes in the experiments shown in H. $n = 3$ per group in which 10 cells were counted per condition per experiment.

Data information: In (C,D,E,J), data are presented as mean ± SEM. $^{*}P \leq 0.05$, $^{**}P \leq 0.01$, $^{***}P \leq 0.001$, $^{****}P \leq 0.0001$, n.s., not significant, calculated by two-tailed Student's *t*-test.

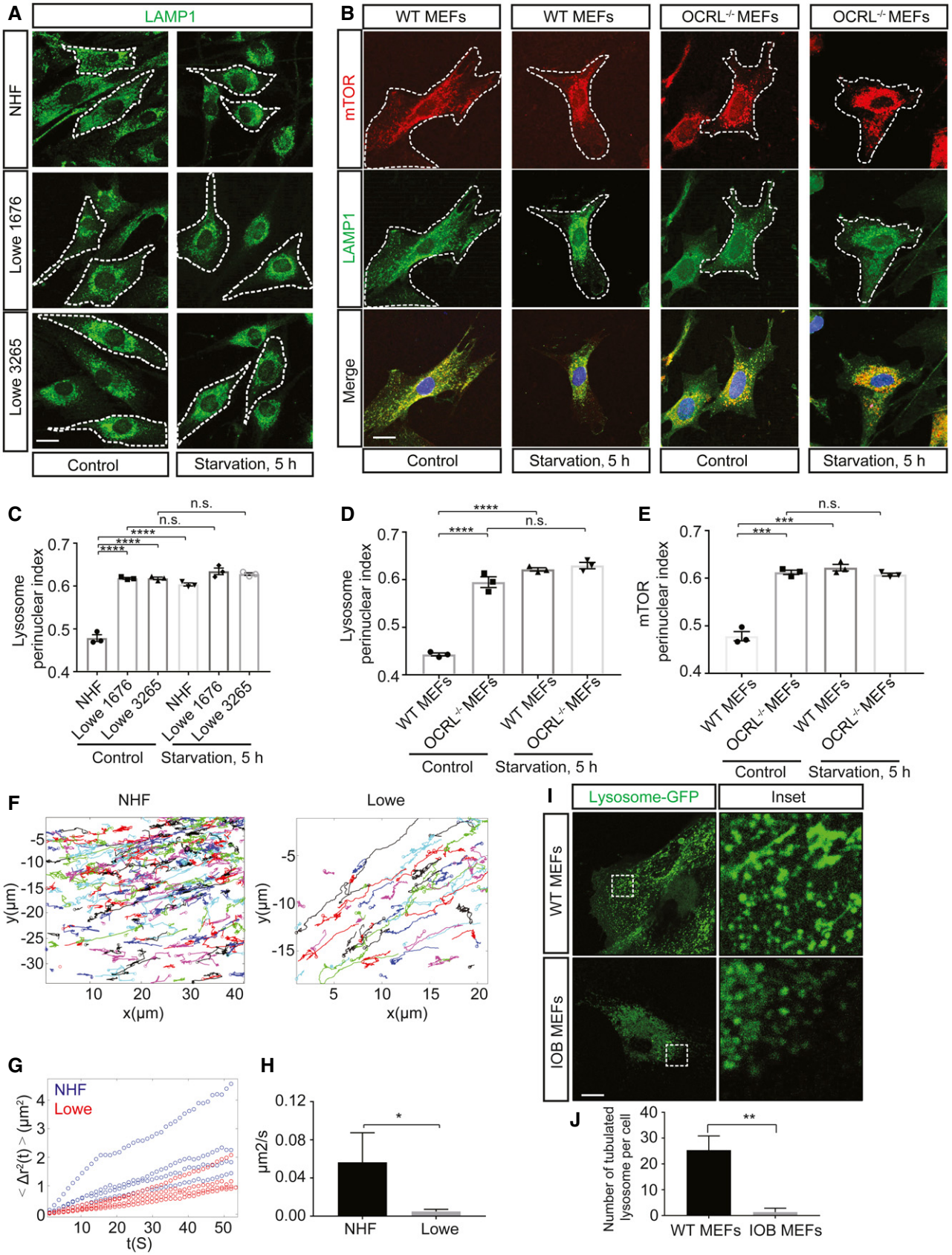
A
LAMP1
NHF
Lowe 1676
Lowe 3265
Control
Starvation, 5 h
B
WT MEFs
WT MEFs
OCRL-/- MEFs
OCRL-/- MEFs
mTOR
LAMP1
Merge
Control
Starvation, 5 h
Control
Starvation, 5 h
C
Lysosome perinuclear index
n.s.
n.s.
****
****
****
NHF
Lowe 1676
Lowe 3265
NHF
Lowe 1676
Lowe 3265
Control
Starvation, 5 h
D
Lysosome perinuclear index
****
****
n.s.
WT MEFs
OCRL-/- MEFs
WT MEFs
OCRL-/- MEFs
Control
Starvation, 5 h
E
mTOR perinuclear index
n.s.
***
***
WT MEFs
OCRL-/- MEFs
WT MEFs
OCRL-/- MEFs
Control
Starvation, 5 h
F
NHF
Lowe
y(μm)
x(μm)
y(μm)
x(μm)
G
NHF
Lowe
< Δr²(t) > (μm²)
t(S)
H
μm2/s
*
NHF
Lowe
I
Lysosome-GFP
Inset
WT MEFs
IOB MEFs
J
Number of tubulated lysosome per cell
**
WT MEFs
IOB MEFs

Figure 1.

and tissues, which could result in serum sensing defects. We also analyzed the effect of both serum and amino acid starvation, which is more physiologic than serum starvation, to further confirm whether decreased mTORC1 activity could affect nutrient sensing. We found that mTORC1 activity was restored significantly more slowly after nutrient replenishment in Lowe patient-derived fibroblasts than in controls, as assayed by the phosphorylation status of S6K and mTOR Ser2448 (Fig 2D–F).

Since mTORC1 functions as a central hub of nutrient signaling and cell growth (Sabatini, 2017; Lawrence & Zoncu, 2019), we next investigated the growth rate of OCRL-deficient cells. We detected a significantly slower growing rate of serum-stimulated IOB MEFs and Lowe patient cells compared with serum-stimulated control NHF cells (Fig 2G and H). Based on the mTORC1 activity phenotype that we observed, we proposed that boosting the activity of mTOR in OCRL-depleted cells might rescue the proliferation defect. For this scope, we used MHY1485, a previously reported cell-permeable mTOR activator which could stimulate mTOR, S6K1, and rpS6 phosphorylation (Cheng *et al,* 2015) and found that it could successfully increase mTORC1 activity in Lowe patient cells (Fig EV2G and H). Treatment with MHY1485 also restored the proliferation rate of Lowe model cells (Fig 2G and H). In support of this, knockdown of TSC2 protein, a well-known negative regulator of mTORC1, also increased the proliferation rate of Lowe model cells (Fig EV2I and J). These results suggested that mTORC1 inactivation was responsible for the difference in proliferation.

Taken together, these results lead us to conclude that the low proliferation rate observed in OCRL-deficient cells was caused by mTORC1 inactivation.

OCRL loss leads to defective centrosomal microtubule nucleation that impairs microtubule-based vesicle transport

Lysosome transport is a microtubule-dependent process (Matteoni & Kreis, 1987). Perinuclear movement of lysosomes, which are typically near the microtubule-organizing center, requires lysosomal calcium channel TRPML1 activity (Li *et al,* 2016). Previous studies have shown that depleting OCRL leads to an accumulation of PI(4,5)P_2 on lysosome membrane, which inhibits lysosomal TRPML1 activity (De Leo *et al,* 2016). Decreased TRPML1 activity should result in peripheral localization of lysosomes (Li *et al,* 2016). However, we and others (De Leo *et al,* 2016) observed lysosomes in the perinuclear region of OCRL-deficient cells (Fig 1A), suggesting that regulation of lysosome positioning occurs by an alternative pathway in this condition. Because in normal conditions lysosomes traffic along microtubules, we hypothesized that there was a microtubule defect in these OCRL-deficient cells. To examine microtubule dynamics in OCRL-deficient cells, we performed immunofluorescence staining of microtubules (α-, β-tubulins) and a centrosome protein (γ-tubulins). We found that OCRL-deficient cells were characterized by non-radial microtubule arrays that failed to anchor to the centrosome, indicating impaired MTOC function (Fig 3A–D). To confirm a possible MTOC abnormality in OCRL-deficient cells, we used siRNA to deplete OCRL in RPE-1 cells (Fig EV3A–D). We verified OCRL depletion with a previously published OCRL antibody (Luo *et al,* 2012) and confirmed the specificity of this antibody using Lowe patient cells (Fig EV3B). We also found that exogenous expression of OCRL could restore microtubule nucleation in Lowe patient cells (Fig EV3E). Proper formation of radial microtubule arrays requires microtubule nucleation. To further assess whether OCRL-deficient cells exhibited defects in MTOC microtubule nucleation, we performed a microtubule regrowth assay. Microtubules depolymerize upon exposure to nocodazole and ice, depolymerization is reversed when cells are restored to 37°C. After 10 min of microtubule regrowth, NHF cells displayed efficient initial nucleation in the form of robust radial microtubule arrays. Lowe patient cells, however, exhibited inefficient initial nucleation with less distinct focal structures (Fig 3E and F). Taken together, these results led us to conclude that OCRL plays a novel role as a microtubule nucleation factor.

We next investigated microtubule dynamics by the transfection of EB3-mCherry, a microtubule plus-end binding protein marker (preprint: Chertkova *et al,* 2017). In RPE cells stably expressing centrin 2-GFP, radial EB3 comets emanated from the centrosome marker (centrin 2), while in OCRL siRNA knockdown cells the EB3 comets around centrin 2 were immobile (Movies EV6 and EV7). In a separate approach, we examined microtubule dynamics in Lowe patient-derived fibroblasts and found immobile perinuclear EB3-mCherry comets (Movies EV8 and EV9). Importantly, the EB3 comets appeared normal in the periphery of OCRL-deficient cells, suggesting that the loss of OCRL only affected the central centrosomal microtubule dynamics (Movies EV8 and EV9). We further examined the effect of the microtubule nucleation defect on the

Figure 2. OCRL deficiency impairs lysosome positioning leading to mTOR inactivation and abnormal nutrient sensing.

A Immunoblot analysis of endogenous p-mTOR (Ser2448), total mTOR, p-p70 S6K (Thr389), and total p70 S6K in NHF, Lowe 1676 and Lowe 3265 cells grown in complete media or 5 h serum starvation. p-p70 S6K (Thr389) over total p70 S6K ratios normalized to NHF cells, three independent experiments.

B Immunoblot analysis of endogenous p-mTOR (Ser2448), total mTOR, p-p70 S6K (Thr389), and total p70 S6K in WT (*Ocrl*$^{+/y}$) and IOB MEFs grown in complete medium or 5 h serum starvation. p-p70 S6K (Thr389) over total p70 S6K ratios normalized to NHF cells, three independent experiments.

C Immunoblot analysis of GFP, p-mTOR (Ser2448), total mTOR, p-p70 S6K (Thr389), and total p70 S6K in Lowe 1676 transfected with or without GFP-OCRL.

D NHF and Lowe 1676 cells were grown in complete media, amino acid (aa)/FBS starved for 5 h, or starved and then recovered in amino acid/FBS-containing medium, then immunoblotted using antibodies against endogenous p-mTOR (Ser2448), total mTOR, p-p70 S6K (Thr389), and total p70 S6K.

E Quantification of p-mTOR (Ser2448) over total mTOR ratios normalized to NHF cells as shown in D, $n = 3$.

F Quantification of p-p70 S6K (Thr389) over total p70 S6K ratios normalized to NHF cells as shown in D, $n = 3$.

G WT and IOB MEFs were grown in 1% FBS, 15% FBS media with or without 2 μmol MHY1485 for 4 days. Relative cell number is the ratio of cells on day 4 normalized to day 1, three independent experiments. ****, $^{\#\#\#\#}P < 0.0001$, calculated by two-way ANOVA.

H NHF and Lowe 1676 cells were grown in 1% FBS, 15% FBS media with or without 2 μmol MHY1485 for 4 days. Relative cell number is the ratio of cells on day 4 normalized to day 1, three independent experiments. ****, $^{\#\#\#\#}P < 0.0001$, calculated by two-way ANOVA.

Data information: In (A–F), data are presented as mean ± SEM. *$P \leq 0.05$, **$P \leq 0.01$, ***$P \leq 0.001$, ****$P \leq 0.0001$, n.s., not significant, calculated by two-tailed Student's *t*-test unless otherwise stated.

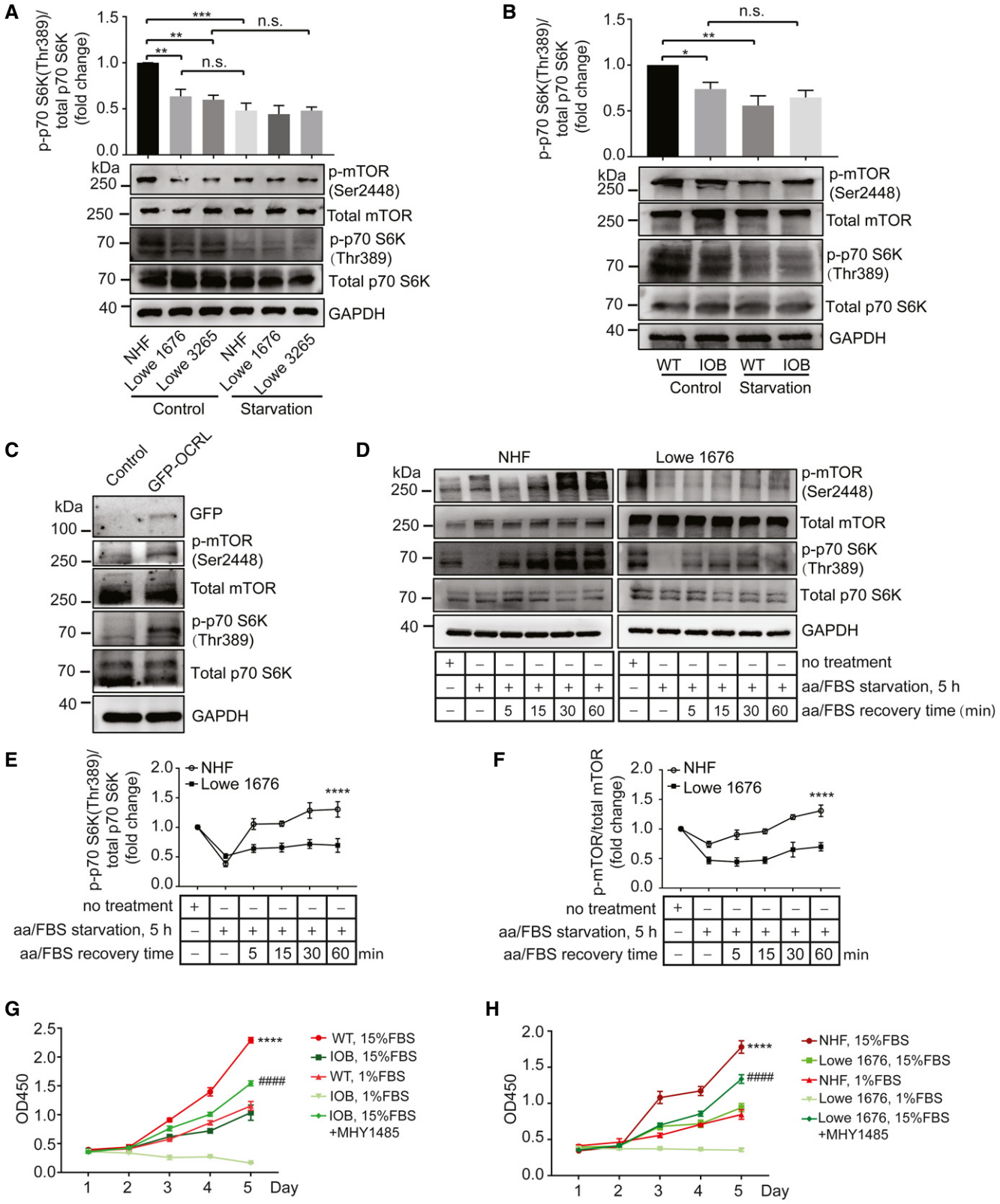

Figure 2.

positioning of early endosomes; this transport is also dependent on microtubules (Cole & Lippincott-Schwartz, 1995). Consistent with our previous findings, EEA1 staining revealed persistent perinuclear early endosome positioning in Lowe patient cells (Fig EV3F). Akt moves to and is activated in EEA1 endosomes (Nazarewicz *et al,* 2009). Perinuclear clustering of early endosomes should result in decreased baseline Akt activity, consistent with published reports (Oltrabella *et al,* 2015) and the current study (Fig EV3G). We also confirmed an additional delay in the recovery of Akt activity under insulin treatment in Lowe patient cells (Fig EV3G).

Collectively, these results indicate that OCRL is required for centrosomal microtubule nucleation and suggest that defects in this process could lead to impaired microtubule-based vesicle transport and aberrant lysosome and early endosome positioning.

OCRL localizes at the proximal end of centrioles via its ASH domain

Microtubule nucleation takes place primarily at centrosomes (Petry & Vale, 2015). We previously reported that OCRL protein is located on cilia under certain conditions and that deficiency of OCRL leads to shortened cilia (Luo *et al,* 2012). Because cilia are centrosome- and microtubule-based structures, we next investigated whether OCRL was specifically localized to the centrioles to regulate centrosomal microtubule nucleation. OCRL distribution was examined in several cell types by immunostaining with a specific OCRL antibody or transfecting with a GFP-OCRL construct. In RPE-1 cells, the immunostaining revealed two prominent regions that co-localized with centriolar protein γ-tubulin (Fig 4A). Costaining OCRL with centrin 2 confirmed this localization (Fig EV4A), and OCRL depletion with siRNA significantly decreased the centrosomal OCRL staining (Fig EV4B). OCRL has been reported to associate primarily with the TGN (Lowe, 2005); our data supported this observation (Fig EV4C). Cells transfected with GFP-OCRL also displayed the centriolar pattern, supporting the specificity of our immunostaining (Fig 4B). We next partially purified the centrosome using a high-speed ultracentrifugation protocol followed by a sucrose gradient and found that OCRL was concentrated in the 50% sucrose centrosomal fraction (Fig 4C), which is similar to the distribution of the centrosomal protein γ-tubulin. The examination of the distribution of OCRL in mitotic cells revealed OCRL co-localized with the centrosome marker in all stages of the cell cycle (Fig 4D). Starvation did not affect the centrosomal OCRL localization (Fig EV4D). Confocal imaging showed that OCRL localized to a specific region of centrosomes, which prompted us to determine its sub-centriolar distribution.

To examine whether OCRL associates preferentially with the mother or daughter centrioles, we examined OCRL immunofluorescence using superresolution, structured illumination microscopy (SIM). Centrioles in RPE-1 cells stably expressing centrin 2-GFP were labeled with the antibody C-Nap1 to mark their proximal ends and with CEP164 to mark their distal appendages. OCRL staining decorated the ends of the centrioles, specifically on opposite sides of the centrin-GFP signal (Fig 4E). Moreover, the OCRL distribution was similar to that of C-Nap1 (Fig 4F), which decorated the proximal end of both mother and daughter centrioles (Fry *et al,* 1998), confirming that OCRL localizes to the proximal region of both mother and daughter centrioles.

The ASH domain of TRAPPII, which was reported to target the protein to the centrosome (Schou *et al,* 2014), is present in OCRL. We therefore investigated the centrosomal targeting role of the ASH domain in OCRL by transfecting RPE-1 cells with OCRL either with the RhoGAP domain truncated or with both the RhoGAP and ASH domains truncated. We found that the single RhoGAP domain truncation did not affect OCRL centrosomal localization. However, the ASH and RhoGAP domain double truncation eliminated the centrosomal OCRL localization (Fig 4H and I), suggesting that the ASH domain is required for OCRL centrosomal localization.

The Rab11–Rabin8–Rab8 signaling pathway, which involves recruitment of Rabin8 and subsequent activation of Rab8, has been implicated in cilia formation and in binding to the OCRL ASH domain (Hagemann *et al,* 2012). We next examined whether Rab8 mediates the centrosomal OCRL localization. Our results showed that OCRL and Rab8 co-localized at the centrosome, suggesting Rab8 as a candidate for transporting OCRL to the centrosome. However, specific depletion of Rab8 from RPE-1 cells with siRNA did not affect the accumulation of centrosome-associated OCRL at either the mother or daughter centriole (Fig EV4E–G).

OCRL deficiency does not affect the centrosomal PI(4,5)P_2 pool

PI(4,5)P_2 (substrate of OCRL) and PI(4)P (product of OCRL) are known to be present in the centrosome (Xu *et al,* 2016); PI(4,5)P_2 has been reported to affect microtubule organization (Gervais *et al,* 2008). With OCRL localized to centrioles (Fig 4E and F), we asked

Figure 3. OCRL deficiency causes failed microtubule nucleation.

A Representative images of NHF, Lowe 1676, and Lowe 3265 cells immunostained with anti-α-tubulin (red) and anti-γ-tubulin (green) antibodies. Scale bar, 10 μm.

B Quantitative analyses of focused microtubule arrays numbers at γ-tubulin (microtubule-organizing center MTOC) measured in the experiments shown in A. $n = 3$ cells per group, three independent experiments.

C WT (*Ocrl*$^{+/y}$), OCRL knockout (*Ocrl*$^{-/-}$), and IOB MEFs derived from the corresponding mice were costained with anti-α-tubulin and anti- γ-tubulin antibodies. Nuclei were stained with DAPI (blue). Scale bar, 10 μm.

D Quantitative analyses of focused microtubule arrays numbers at γ-tubulin (microtubule-organizing center MTOC) measured in the experiments shown in C. $n = 3$ per group in which 30 cells were counted per condition per experiment.

E Microtubule regrowth assay was performed on NHF, Lowe 1676, and Lowe 3265 cells with 20 μM nocodazole for 2 h on ice, followed by rinse with PBS, and addition of pre-warmed medium to induce microtubule regrowth. Cells were then immunostained with anti-α-tubulin and anti-γ-tubulin antibodies at the indicated time point after addition of pre-warmed medium. The magnified view shows the cytoplasmic microtubules organization center. Scale bar, 10 μm.

F Quantitative analyses of focused microtubule arrays numbers at γ-tubulin (microtubule-organizing center, MTOC) measured in the experiments shown in E. $n = 3$ per group in which 30 cells were counted per condition per experiment.

Data information: In (B,D,F), data are presented as mean ± SEM. *$P \leq 0.05$, **$P \leq 0.01$, calculated by two-way ANOVA, multiple comparisons.

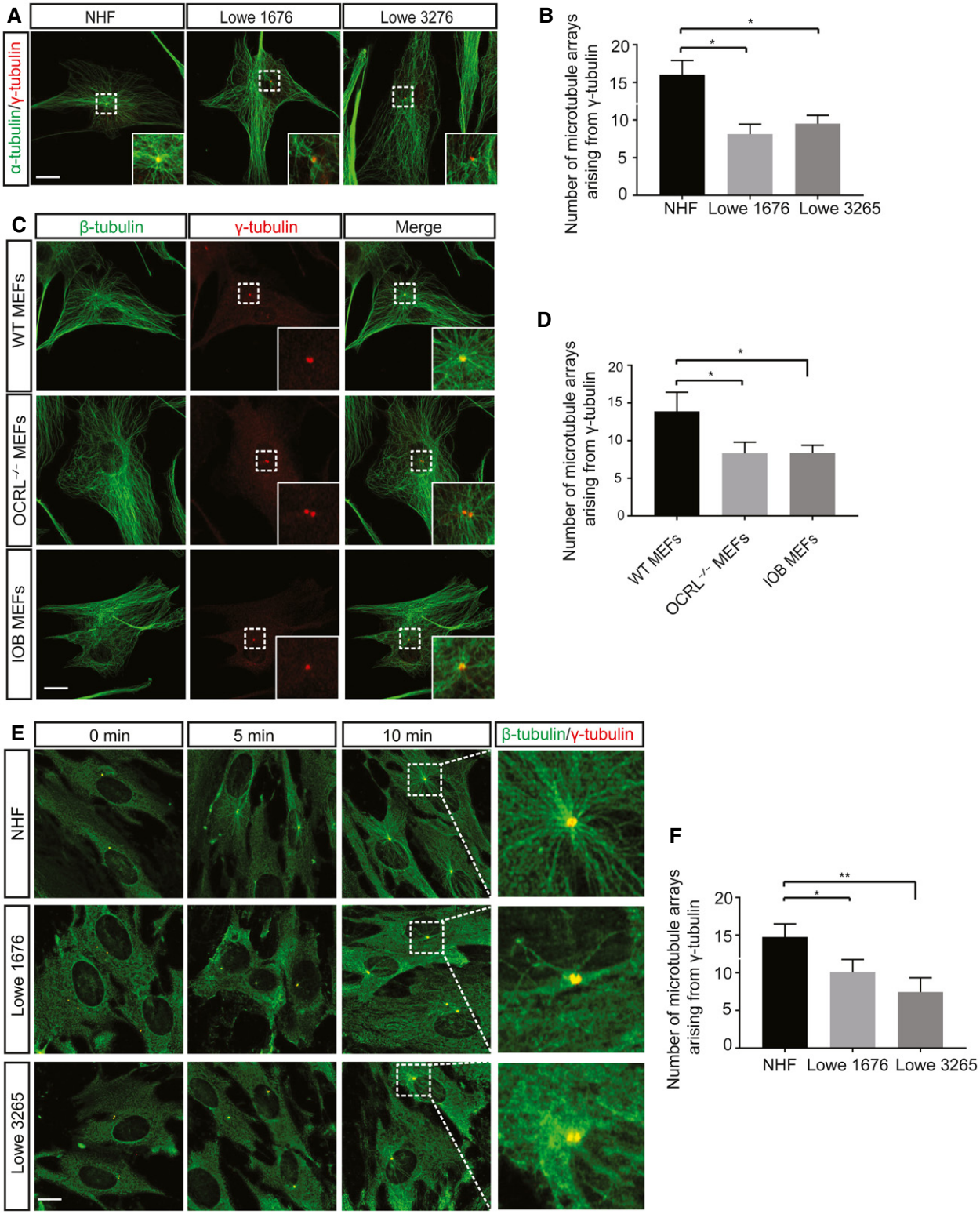

Figure 3.

whether OCRL could be involved in the regulation of centrosomal PI(4,5)P_2, and subsequent regulation of microtubule nucleation. To test this hypothesis, we first investigated the centrosomal PI(4,5)P_2 expression level in OCRL-depleted RPE-1 cells. As shown in Fig 5A, monoclonal PI(4, 5)P_2 antibody clearly decorated the centrosomes in RPE −1 cells; however, we did not observe specific centrosome accumulation of PI(4,5)P_2 in OCRL siRNA knockdown cells (Figs 5A and B, and EV5A and B). Furthermore, no notable differences could

be detected in antibody staining of $PI(4,5)P_2$ between NHF and Lowe cells (Fig 5C and D). In a separate approach, we transfected cells with PH-PLCdelta-GFP, a fluorescent translocation biosensor, to monitor changes or local differences in $PI(4,5)P_2$ lipids (Balla & Varnai, 2002); we did not observe any accumulation of the centrosomal $PI(4,5)P_2$ in Lowe patient cells during interphase (Fig EV5C). In addition, we did not find that centrosomal $PI(4,5)P_2$ expression levels differed between Lowe patient cells and NHF cells during mitosis (Fig EV5D). We therefore concluded that centrosomal OCRL did not directly affect centrosomal $PI(4,5)P_2$ levels.

OCRL-deficient cells fail to recruit microtubule-anchoring factor SSX2IP

Because the OCRL protein does not contain classical microtubule-binding sites, we searched for OCRL interacting proteins that might mediate microtubule nucleation. Of the 54 OCRL interacting proteins included on BioGRID3.5, SSX2IP is the only binding protein reported to play a role in microtubule anchoring (Hori *et al*, 2014). Therefore, we tested whether OCRL deficiency leads to SSX2IP dysfunction. The interaction between OCRL and SSX2IP in RPE cells was confirmed by co-immunoprecipitation (Fig 6A). Protein-docking predictions using the ClusPro program indicated that the ASH domain of OCRL might mediate the interaction with SSX2IP (Appendix Fig S1A). We also found that a RhoGAP domain single truncation could eliminate the interaction between OCRL and SSX2IP (Fig 6A), suggesting that the RhoGAP domain is of equal importance for the interaction. In normal human fibroblasts, SSX2IP was present in both the cytosol and the centrosomes. Intriguingly, we found significant loss of centrosomal SSX2IP in OCRL knockout MEFs (Fig 6B and C) and decreased centrosomal SSX2IP in Lowe patient cells (Appendix Fig S1B and C). We hypothesized that restoration of SSX2IP to the centrosome using a PACT domain from AKAP450 fused to GFP-SSX2IP, which has been reported to target the protein to the centrosome (Gillingham & Munro, 2000), would rescue the OCRL-deficient phenotype. Exogenous expression of GFP-PACT-SSX2IP, but not of wild-type GFP-SSX2IP, restored MTOC function of microtubules in Lowe patient cells (Fig 6D and E), supporting the idea that loss of centrosomal SSX2IP is the underlying mechanism for MTOC loss in OCRL-deficient cells. Importantly, the centrosome-targeted GFP-PACT-SSX2IP but not the wild-type GFP-SSX2IP ameliorated the observed mTORC1 defect in Lowe patient cells (Fig 6F and D, Appendix Fig S1). In addition, we showed that knockdown of endogenous SSX2IP leads to a decrease in mTORC1 activity, lysosome mobility, and cell proliferation rate in NHF cells (Appendix Fig S1, Fig 6E–H), which resembles the phenotypes observed in OCRL-deficient cells. Most importantly, reintroducing PACT-SSX2IP could rescue the lysosome mobility defects, nutrient sensing, and cell proliferation rate in Lowe 1676 cells (Appendix Fig S1, Fig 6I–K).

In conclusion, our data showed that OCRL binds to SSX2IP through its RhoGAP domain and plays a critical role in MTOC formation and microtubule-based vesicle movement.

Discussion

The ability of OCRL to regulate lysosome positioning and mTORC1 activity highlights for the first time a novel pathway that contributes to the pathophysiological alterations observed in Lowe syndrome (Fig 6G). Lysosomes are cytoplasmic organelles responsible for degrading various macromolecules produced in cells and for another metabolic signaling (Lawrence & Zoncu, 2019). Because the involvement of lysosomes in these processes depends on their ability to move along microtubules, the mechanisms regulating lysosome positioning are critical in the maintenance of normal cellular functions. Although alterations of lysosome size and number were described previously in Lowe syndrome (De Leo *et al*, 2016), we now report a significant alteration in lysosome positioning in this disease. The present study is the first to provide evidence to show a distinct pathway through which OCRL-dependent microtubule nucleation precisely regulates lysosome positioning.

Microtubules have an important role in providing tracks for motor-driven transport to position most cell membrane-bound organelles (Caviston & Holzbaur, 2006). Previous studies showed that perinuclear lysosome clustering is a microtubule-dependent process and that depolymerization of the whole cellular microtubule network by nocodazole scatters the distribution of lysosomes

Figure 4. OCRL localizes to the proximal end of centrioles.

A Representative images of RPE-1 cells costained with anti-OCRL (red) and anti-γ-tubulin (green) antibodies. Insets show the enlarged centrosomal region. Scale bar, 10 μm.

B Representative images of the co-localization of GFP-OCRL-WT (green) with centrosome marker γ-tubulin (red) in RPE-1 cells. Insets show the enlarged centrosomal region. Scale bar, 10 μm.

C The purified centrosome fraction (50%) isolated from RPE-1 cells and the cell lysate (5%) were subjected to immunoblot analysis with anti-OCRL antibody. The centrosomal protein γ-tubulin was probed as control.

D Representative images of RPE-1 cells costained with anti-OCRL (red) and anti-γ-tubulin (green) antibodies during mitosis. Insets show the enlarged centrosomal region. Scale bar, 2 μm.

E Super-resolution images of centrosome stained with anti-CEP164 (red, labeling distal appendages of mother centriole) and anti-OCRL (blue) were acquired using centrin 2-GFP-RPE-1 cells by DeltaVision OMX V4 BLAZE system. Scale bar, 0.5 μm.

F Super-resolution images of centrosome stained with anti-CNAP1 (red, labeling proximal ends of centriole) and anti-OCRL (blue) were acquired using centrin 2-GFP-RPE-1 cells by DeltaVision OMX V4 BLAZE system. Scale bar, 0.5 μm.

G Model depicting the localization of the OCRL on mother and daughter centrioles.

H Representative images of the co-localization of OCRL-WT, GFP-OCRL-△RhoGAP, and GFP-OCRL-△ASH+RhoGAP with γ-tubulin. Insets, enlargements of the outlined areas. Scale bars, 10 μm.

I Quantitative analysis of cells with and without centrosomal OCRL (centrosomal GFP signal) in the experiments shown in A. $n = 3$ per group in which 10 cells were counted per condition per experiment. Means ± SEM, $^{****}P < 0.0001$, n.s., not significant, calculated by two-way ANOVA, multiple comparisons.

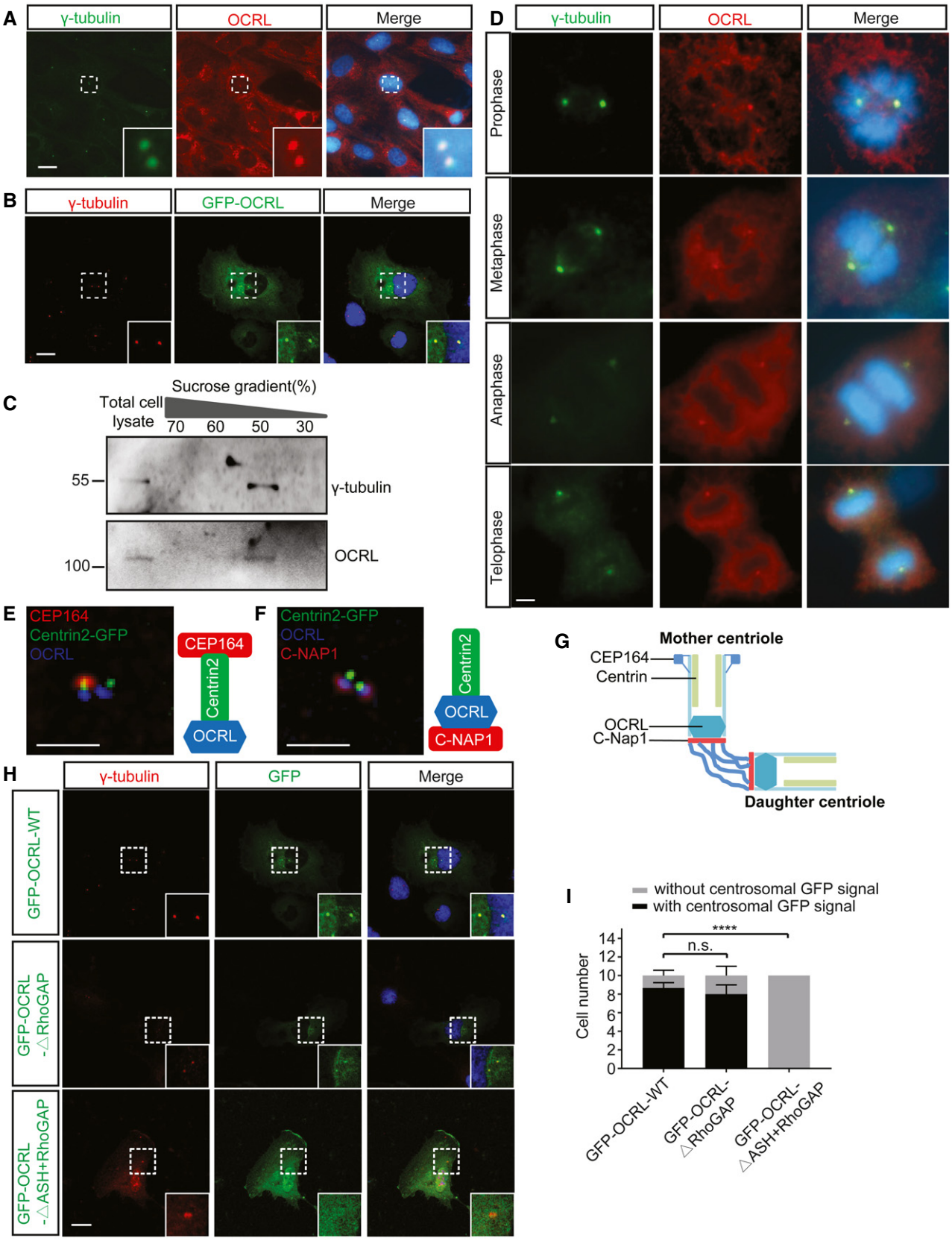
A
γ-tubulin
OCRL
Merge
B
γ-tubulin
GFP-OCRL
Merge
C
Sucrose gradient(%)
Total cell lysate
70 60 50 30
55
γ-tubulin
100
OCRL
D
γ-tubulin
OCRL
Merge
Prophase
Metaphase
Anaphase
Telophase
E
CEP164
Centrin2-GFP
OCRL
CEP164
Centrin2
OCRL
F
Centrin2-GFP
OCRL
C-NAP1
Centrin2
OCRL
C-NAP1
G
Mother centriole
CEP164
Centrin
OCRL
C-Nap1
Daughter centriole
H
γ-tubulin
GFP
Merge
GFP-OCRL-WT
GFP-OCRL -△RhoGAP
GFP-OCRL -△ASH+RhoGAP
I
without centrosomal GFP signal
with centrosomal GFP signal
Cell number
****
n.s.
GFP-OCRL-WT
GFP-OCRL-△RhoGAP
GFP-OCRL-△ASH+RhoGAP

Figure 4.

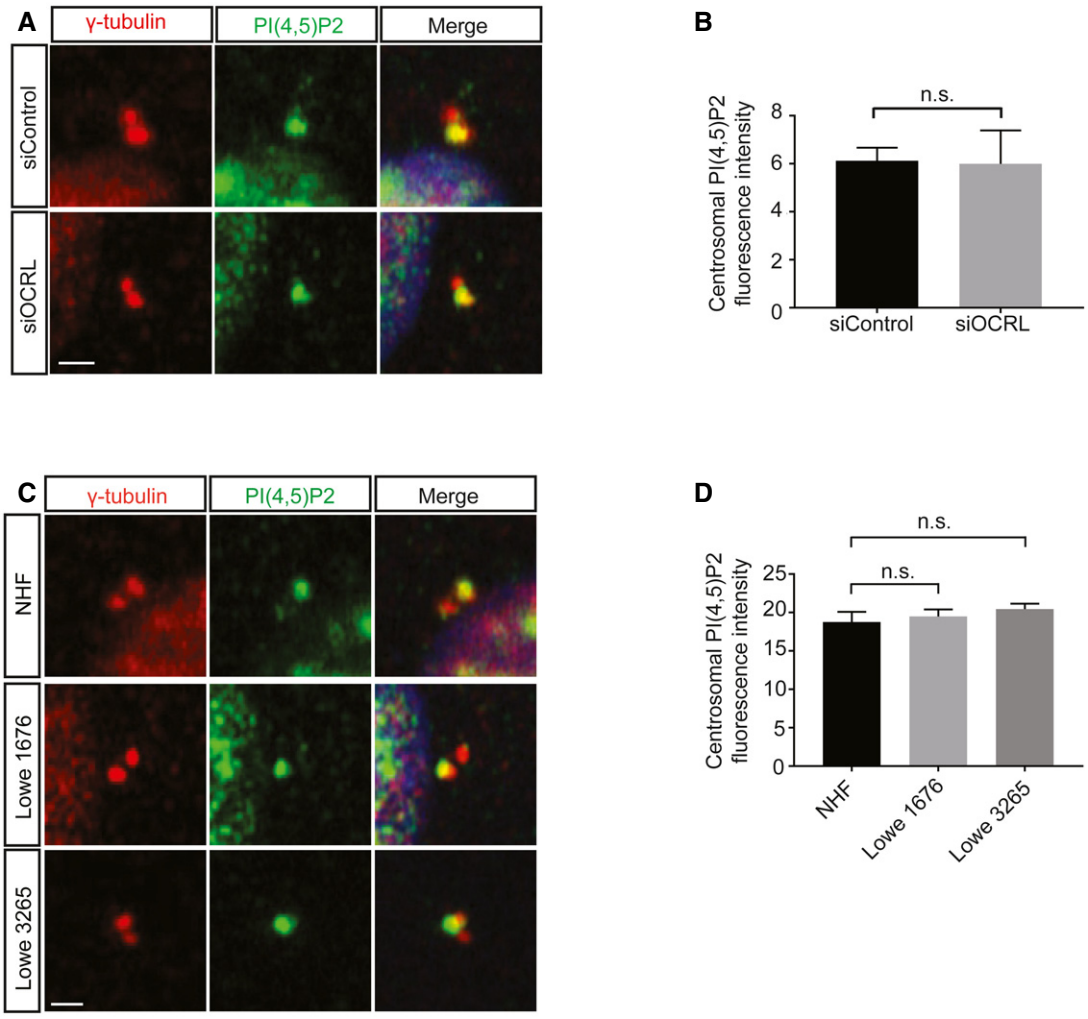

Figure 5. OCRL deficiency does not affect centrosomal PI(4,5)P_2 pool.

A RPE-1 cells transfected with nontargeting control siRNA or OCRL siRNA were left for 48 h, then subjected to IF microscopy to visualize PI(4,5)P_2 (green), γ-tubulin (red), and nuclei (blue, DAPI staining). Scale bar, 10 μm.

B Quantitative analyses of centrosomal PI(4,5)P_2 fluorescence intensity in the experiments shown in A. $n = 3$ per group in which 50 cells were counted per condition per experiment.

C NHF, Lowe 1676, and Lowe 3265 cells were subjected to IF microscopy to visualize PI(4,5)P_2 (green), gamma-tubulin (red), and nuclei (blue, DAPI staining). Scale bar, 10 μm.

D The fluorescence intensity of PI(4,5)P_2 on centrosomes in C was measured. $n = 3$ per group in which 50 cells were counted per condition per experiment.

Data information: In (B,D), data are presented as mean ± SEM. n.s., not significant, calculated by calculated by two-tailed Student's *t*-test.

(Matteoni & Kreis, 1987; Korolchuk *et al*, 2011). Here, we showed evidence that OCRL-mediated disruption of microtubules nucleated from the centrosome causes perinuclear clustering of lysosomes. Centrosomal microtubule nucleation is significantly decreased in OCRL-deficient human cells, but these cells retain a diminished microtubule network (Fig 3A–D). However, the microtubule network was totally lost in cells treated with nocodazole (Fig 3E). Golgi, kinetochores, and even pre-existing microtubules have been reported to be able to function as MTOCs (Petry & Vale, 2015). Since centrosomes are not the only MTOC in the cell, it is possible that decreased centrosomal microtubule nucleation in OCRL-deficient cells may only affect vesicle trafficking in the perinuclear region, where the centrosome MTOC is located. Our results using EB3-mcherry to track microtubule dynamics in OCRL-depleted cells showed that OCRL depletion produces marked disorganization and perinuclear accumulation of EB3 comets. The EB3 distribution overlaps with the perinuclear accumulation of lysosomes, supporting the notion that the impaired lysosome positioning is due to disorganized microtubule dynamics around the centrosomes. However, the differences between the effects of the centrosome-based microtubule network and the Golgi-based microtubule network in positioning cellular organelles are unclear, and how these two different networks interact with each other is still unknown. Thus, future studies are needed to resolve these questions.

Our study shows that OCRL is localized to the centrosome via its ASH domain and that it recruits the microtubule-anchoring factor

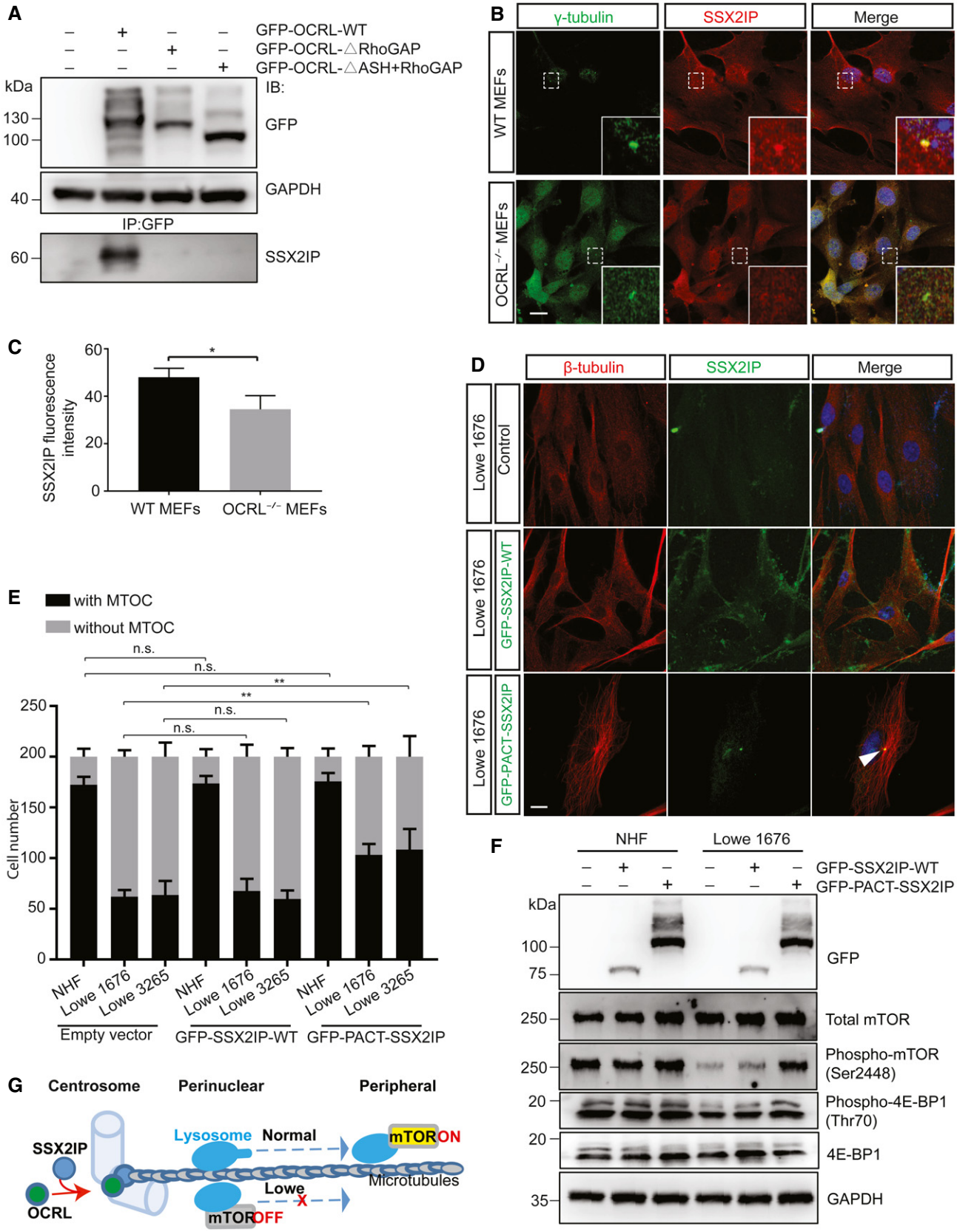
A
GFP-OCRL-WT
GFP-OCRL-△RhoGAP
GFP-OCRL-△ASH+RhoGAP
kDa
130
100
40
60
IB:
GFP
GAPDH
IP:GFP
SSX2IP
B
γ-tubulin
SSX2IP
Merge
WT MEFs
OCRL−/− MEFs
C
SSX2IP fluorescence intensity
WT MEFs
OCRL−/− MEFs
D
β-tubulin
SSX2IP
Merge
Lowe 1676
Control
GFP-SSX2IP-WT
GFP-PACT-SSX2IP
E
with MTOC
without MTOC
Cell number
n.s.
**
NHF
Lowe 1676
Lowe 3265
Empty vector
GFP-SSX2IP-WT
GFP-PACT-SSX2IP
F
NHF
Lowe 1676
GFP-SSX2IP-WT
GFP-PACT-SSX2IP
kDa
GFP
Total mTOR
Phospho-mTOR (Ser2448)
Phospho-4E-BP1 (Thr70)
4E-BP1
GAPDH
G
Centrosome
Perinuclear
Peripheral
SSX2IP
OCRL
Lysosome
Normal
mTORON
Lowe
mTOROFF
Microtubules

Figure 6.

Figure 6. OCRL mediates microtubule nucleation through SSX2IP.

A SSX2IP interacts with OCRL. Plasmids carrying GFP-OCRL-WT, GFP-OCRL-△RhoGAP, and GFP-OCRL-△ASH+RhoGAP were transfected into RPE-1 cells. Immunoprecipitation was performed with GFP-Trap, followed by blotting with the indicated antibodies.

B WT (*Ocrl*$^{+/y}$) and OCRL knockout (*Ocrl*$^{-/-}$) MEFs were costained with anti-SSX2IP and anti-γ-tubulin antibodies. Nuclei were stained with DAPI (blue). Insets show the enlarged centrosomal region. Scale bar, 5 μm.

C Quantification of centrosomal fluorescence intensity of SSX2IP in the experiments shown in B. $n = 3$ per group in which 50 cells were counted per condition per experiment.

D NHF, Lowe 1676, and Lowe 3265 cells were transfected with wild-type GFP-SSX2IP or GFP-PACT-SSX2IP for 48 h, then immunostained with anti-β-tubulin (red) antibody. Nuclei (blue) were stained with DAPI. The centrosomal microtubule nucleation in GFP-PACT-SSX2IP transfected cells was indicated by white arrowhead. Scale bar, 5 μm.

E Quantitative analyses of cells with and without MTOC. NHF, Lowe 1676, and Lowe 3265 cells were transfected with wild type GFP-SSX2IP or GFP-PACT-SSX2IP for 48 h, then immunostained with anti-γ-tubulin (red) antibody. Nuclei (blue) were stained with DAPI. $n = 3$ per group in which 10 cells were counted per condition per experiment.

F Western blot analysis of GFP, endogenous phospho-mTOR, total mTOR, in NHF and Lowe 1676 cells. NHF and Lowe 1676 cells were left untransfected, transfected with GFP-SSX2IP-WT or GFP-PACT-SSX2IP, then immunoblotted with indicated antibodies.

G Diagram illustrating that in normal conditions, OCRL recruits SSX2IP to the centrosomes, thus maintaining microtubule nucleation. Nucleated microtubules allow transport of perinuclear lysosomes to the cell periphery to activate mTOR activity. OCRL deficiency in Lowe syndrome causes a significant loss of microtubule nucleation and a marked perinuclear accumulation of lysosomes, which leads to mTOR inactivation.

Data information: In (C), data are presented as mean ± SEM. *$P \leq 0.05$, calculated by two-tailed Student's *t*-test. In (E), data are presented as mean ± SEM. **$P \leq 0.01$, calculated by two-way ANOVA, multiple comparisons.

SSX2IP to promote microtubule nucleation for MTOC formation. The ASH domain was first identified by *in silico* analysis in proteins associated with cilia and the centrosome (Ponting, 2006; Schou *et al,* 2014). The ability of OCRL to regulate microtubule anchoring to the centrosome appears critical to normal cellular function. OCRL is located on the mother centriole, which functions as the basal body of the primary cilium. Because cilia formation requires microtubule anchoring to the basal body, the contribution of OCRL to microtubule anchoring can explain why OCRL deletion causes cilia shortening in Lowe syndrome. The mechanism responsible for cilia shortening remains unknown. OCRL mutations cause loss of enzymatic activity in patients with Lowe syndrome, and the centrosomal function of OCRL in PI(4,5)P_2 hydrolysis could be important for the effects of the disease. However, we did not observe any significant accumulation of PI(4,5)P_2 in centrosomes of OCRL-deficient cells, suggesting that the non-phosphatase function of OCRL may be important for centrosomal regulation. Previous studies have shown that SSX2IP promotes centrosome maturation and that SSX2IP depletion leads to disorganized interphase microtubules with reduced length and intensity (Barenz *et al,* 2013; Hori *et al,* 2014). This phenotype overlaps with that of OCRL-depleted cells, indicating that the function of OCRL at the centrosome is tightly associated with SSX2IP. Furthermore, knockdown of the SSX2IP orthologue impairs ciliary formation during zebrafish embryogenesis (Hori *et al,* 2014), as does OCRL knockdown in a zebrafish model (Luo *et al,* 2012). These findings strongly support an overlapping function between OCRL and SSX2IP.

It is well known that lysosome positioning in cells is important in the coordination of mTORC1 signaling (Korolchuk *et al,* 2011; Lawrence & Zoncu, 2019). Our immunoblot analysis showed that the total mTORC1 level was decreased in OCRL-deficient cells, suggesting that one of the major pathways affected by defective OCRL function leads to impaired activation of this kinase complex. Consistent with the present results, the expression and activity of Rac1, an important mTORC1 regulator that localizes with mTORC1 in both nutrient and starvation conditions, are also reported to be significantly decreased in Lowe syndrome patient cells (Saci *et al,* 2011; Madhivanan *et al,* 2012). Our observation that the reintroduction of GFP-PACT-SSX2IP specifically rescues the activity of mTORC1 supports the idea that SSX2IP acts downstream of OCRL in regulating mTORC1 activity. Importantly, our discovery that the mTOR activator MHY1485 restores the nutrient sensing ability of Lowe model cells suggesting that this pathway could be a promising therapeutic target for Lowe syndrome.

Materials and Methods

Reagents and Tools table

Reagent/Resource	Reference or Source	Identifier or catalog number
Experimental models		
C57BL/6J (M. musculus)	Jackson Lab	B6.129P2Gpr37tm1Dgen/J
Ocrl$^{-/-}$ *Inpp5b*$^{-/-}$ *INPP5B*$^{+/+}$ (IOB)	Robert L. Nussbaum (University of California, San Francisco)	
Ocrl$^{-/-}$	Robert L. Nussbaum (University of California, San Francisco)	
hTERT RPE-1	ATCC	CRL-4000
hTERT RPE-1 stably expression centrin2-GFP	Tim Stearns Lab(Stanford University, Palo Alto)	

Reagents and Tools table (continued)

Reagent/Resource	Reference or Source	Identifier or catalog number
Recombinant DNA		
GFP-SSX2IP	Laurence Pelletier's group (University of Toronto, Toronto, Canada)	
GFP-PACT-SSX2IP	Laurence Pelletier's group (University of Toronto, Toronto, Canada)	
GFP-OCRL-WT	Yang Sun Lab (Stanford University School of Medicine, California, USA)	
GFP-OCRL-D499A	Yang Sun Lab (Stanford University School of Medicine, California, USA)	
GFP-OCRL-△RhoGAP	Yang Sun Lab (Stanford University School of Medicine, California, USA)	
GFP-OCRL-△ASH+RhoGAP	Yang Sun Lab (Stanford University School of Medicine, California, USA)	
CellLight™ Lysosomes-GFP, BacMam 2.0	Thermo Fisher Scientific	C10596
CellLight™ Lysosomes-RFP, BacMam 2.0	Thermo Fisher Scientific	C10504
mCherry-EB3-C-20	Addgene	55038
Antibodies		
Anti-OCRL mouse antibody (N166A/26)	UC Davis/NIH NeuroMab Facility	N166A/26
Anti-OCRL mouse antibody (11993)	Homemade	
Anti-SSX2IP (EB06302)	Everest Biotech	EB06302
Anti-SSX2IP (13694-1-AP)	Proteintech	13694-1-AP
Anti-Rab 8A (D22D8)	Cell Signaling Technology	6975
Anti-Rab 8B (11792-1-AP)	Proteintech	11792-1-AP
Anti-γ-tubulin (Poly6209)	BioLegend	Poly6209
Anti-C-NAP-1	Proteintech	14498
Anti-CEP164	Proteintech	22227-1-AP
Anti-LAMP1 antibody (1D4B)	Abcam	ab25245
Anti-mTOR (D95F2)	Cell Signaling Technology	9367
Anti-phospho-mTOR (Ser2448)	Cell Signaling Technology	2971
Anti-p-p70 S6K (Thr389)	Cell Signaling Technology	9205
Anti-p70 S6 Kinase (49D7) Rabbit mAb	Cell Signaling Technology	2708
Anti-4E-BP1 (53H11) Rabbit mAb	Cell Signaling Technology	9644
Anti-Phospho-4E-BP1 (Thr70) Antibody	Cell Signaling Technology	9455
Anti-GAPDH	Santa Cruz Biotechnology	sc-32233
Anti-Tuberin/TSC2 (D93F12) XP® Rabbit mAb	Cell Signaling Technology	4308
Anti-GFP	Proteintech	50430-2-AP
Oligonucleotides and sequence-based reagents		
OCRL siRNA	Dharmacon	D-010026-01-0005
SSX2IP siRNA	Dharmacon	L-020361-01-0005
Rab8A siRNA	Dharmacon	D-003905-01-0005
Rab8B siRNA	Dharmacon	D-008744-02-0005
SignalSilence® Tuberin/TSC2 siRNA I	Cell Signaling Technology	6476
Chemicals, enzymes and other reagents		
MHY1485	Sigma-Aldrich	SML0810-5MG
Nocodazole	Sigma-Aldrich	31430-18-9
YU142670	Sigma-Aldrich	SML1806-5MG
Software		
ImageJ	NIH	
SoftWoRx 3.7	Applied Precision	
ClusPro2.0	https://cluspro.bu.edu/publications.php	
Photoshop	Adobe	

Reagents and Tools table (continued)

Reagent/Resource	Reference or Source	Identifier or catalog number
Other		
Zeiss LSM880 Micoscope	Zeiss	
DeltaVision OMX V4 BLAZE system	Applied Precision	

Methods and Protocols

Reagents

The antibodies and chemicals used in the study are listed in Appendix Table S1, including the clone name, catalog numbers, and commercial providers.

Animals

All animal experiments followed the guidelines of the Association for Research in Vision and Ophthalmology Statement for the Use of Animals in Ophthalmic and Vision Research and were approved by the Institutional Animal Care and Use Committee (IACUC) of Stanford University School of Medicine. *Ocrl*$^{-/-}$ and *Ocrl*$^{-/-}$ *Inpp5b*$^{-/-}$ *INPP5B*$^{+/+}$ (IOB) mice were a gift from Robert L. Nussbaum (University of California, San Francisco). Wild-type (C57BL/6) mice obtained from The Jackson Laboratories were used as control for Ocrl$^{-/-}$ and IOB mice. Animals were housed under a 12-h light/dark cycle with free access to water and food. Mice were anesthetized using isoflurane. Oxygen flow was set to 2 l per minute and isoflurane at 1% under a nose cone.

Cell culture

Cell lines were grown according to American Type Culture Collection. Control human fibroblast cultures (NHF558), Lowe 1676, Lowe 3265, wild-type mouse embryonic fibroblasts (MEFs), OCRL$^{-/-}$ MEFs, and IOB MEFs were maintained in DMEM (10013CV; Corning) supplemented with 15% FBS (F7524; Sigma-Aldrich), 100 U/ml penicillin, and 100 μg/ml streptomycin at 37°C with 5% CO_2. hTERT-RPE-1 cells and hTERT-RPE-1-centrin 2- GFP (gift from Tim Stearn's lab, Stanford University, Palo Alto, CA) were grown in DMEM (10013CV; Corning), 10% FBS. For starvation experiments, cells were grown in DMEM (17207CV; Corning) without FBS.

siRNA transfections

Cells were seeded and transfected with siRNA duplexes using Lipofectamine LTX transfection reagent (13778; Thermo Fisher Scientific) following the manufacturer's instructions. The final concentration of siRNA duplexes was 50 nM. Cells were analyzed 48 h after transfection. Targeted protein silencing was accomplished with siRNA against human OCRL (D-010026-01-0005) or Rab8A (D-003905-01-0005), and Rab8B (D-008744-02-0005) from Dharmacon.

DNA plasmid and transfection

All plasmids were generated by standard molecular biological methods. GFP-SSX2IP and GFP-PACT-SSX2IP were gifts from Laurence Pelletier's group (University of Toronto, Toronto, Canada).

Immunoprecipitation

Briefly, the respective GFP-tagged constructs were transfected into HEK293T cells using lipofectamine LTX (15338100, Thermo Fisher Scientific), and the cells were incubated for 48 h, followed by lysis in RIPA lysis buffer (89900, Thermo Fisher Scientific) and precipitation of GFP with GFP-trap beads (gta-10, Chromotek) for 3 h at 4°C. The protein–beads complexes were then washed with lysis buffer, dissolved in loading buffer, and subjected to immunoblot analysis.

Immunoblot analysis

Cell lysates were exposed to loading buffer. Equal amounts of protein were run on 10–12% gels and transferred to nitrocellulose membranes (Bio-Rad). Membranes were blocked in 5% (vol/vol) nonfat dried milk in PBS. Primary and secondary antibodies were diluted in the concentration 1:1,000. An Odyssey Imaging system (Li-Cor Bioscience) was used to analyze the immunoblots.

Immunofluorescence

Briefly, cell culture slides were treated with 4% PFA for fixation for 10 min at room temperature followed by permeabilization with 0.5% Triton X-100. Samples were then blocked with PBS / 0.5% BSA /10% normal goat serum for 30 min at room temperature. Primary antibodies were applied at 4°C overnight, followed by secondary antibodies at room temperature for 1 h. Imaging was performed with a Zeiss LSM880. For endogenous OCRL staining, ice cold acetone:methanol (1:1) fixation was used to fix cell culture slides. For imaging centrosome-associated PIP2, pre-extract cells were placed in 0.2% Triton X-100 (prepared in PBS) for 30 s (or up to 1 min) at room temperature, then Triton solution was aspirated, and the cells fixed in 4% paraformaldehyde (prepared in PBS) at room temperature for 10 min. Cells were washed once in PBS and stored in PBS at 4°C.

Quantification of lysosome, mTOR, and EEA1 distribution

Average LAMP1 or mTOR intensities were measured for the whole cell (A_{total}) and the area within 10 μm of the nucleus ($B_{perinuclear}$), the perinuclear index, was defined as $B_{perinuclear}$ / A_{total}.

Cell proliferation assay

Cells were seeded at the density of 5,000 cells/well in 96-well plates. In vitro cell proliferation was assessed by Cell Counting Kit-8 (CCK-8) (Dojindo, Tokyo, Japan) according to the manufacturer's instructions.

EB3 live cell imaging

To examine MT dynamics, cells were transfected with EB3-mCherry as previously published (preprint: Chertkova *et al*, 2017). Briefly, time-lapse imaging was performed using a Zeiss LSM880 confocal microscope at 1 frame/s for 120 s and 1 frame/2 s, respectively. The speed and growth of EB3-mCherry mobile comets were obtained with ImageJ (NIH).

Microtubule regrowth assay

Briefly, cells were incubated with 20 μM nocodazole for 2 h on ice, rinsed with PBS, then pre-warmed medium was added to induce MT regrowth. At appropriate time points (0, 5 and 10 min) after addition of pre-warmed medium, cells were processed for immunofluorescence microscopy.

SIM microscopy

The SIM micrographs were acquired using a DeltaVision OMX V4 BLAZE system (Applied Precision, Issaquah, WA). The microscope was equipped with a 100×/1.42 NA U-PLANAPO SIM oil immersion objective (Olympus, Tokyo, Japan), 405-, 488-, 568-, and 642-nm lasers, and three EMCCD cameras. The sequential imaging mode was used to acquire images. An electro-optical high-speed SI diffraction grating engine was used to generate SI patterns. Image stacks were composed of 15 images/plane, sectioning with a z-distance of 0.125 μm, and spanning a total distance of 4–8 μm for tissue culture cells. The resulting images were computationally reconstructed, generating superresolution optical serial sections with twofold extended resolution in all three axes. Color channels were aligned computationally, using measurements taken with 0.1-μm multispectral fluorescent beads (Tetraspeck beads; Invitrogen) as a control. The SoftWoRx 3.7 imaging software package (Applied Precision) was used for SI reconstruction and image processing. All images were processed using Fiji (National Institutes of Health, Bethesda, MD) and/or Photoshop (Adobe, San Jose, CA).

Centrosome isolation

Cells were treated with 1 M cytochalasin D and 3.3 μM nocodazole for 1 h before harvesting. A total of 2×10^8 cells were lysed in hypotonic lysis buffer (1 mM Tris pH 8.0, 0.1% v/v β-mercaptoethanol), 0.5 % v/v NP-40, 0.5 mM $MgCl_2$, 150 μl of 20,000 U DNase I), and centrifuged through a 2 ml 50% w/w sucrose cushion. The cushion–lysate interface was further subjected to a discontinuous gradient sucrose centrifugation (70, 60, 50, and 30% w/w sucrose). Isolated centrosomes from each of the fractions were pelleted through 10 mM PIPES and subjected to western blot analysis.

Protein-docking predictions for OCRL and SSX2IP

Since the ASH-RhoGAP module of the OCRL protein mediates a majority of the known protein–protein interactions and the sequence is homology to coiled-coil domains, we modeled residues 105–311 of OCRL using homology modeling. This portion of the OCRL was used as an input for protein-docking predictions by ClusPro. The top scoring predicted complex is presented.

Single particle tracking of lysosomal trajectories

Trajectories of lysosomes in Lowe 1676 and NHF cells were obtained as described (He *et al*, 2016) and labeled in different colors with the same colored circles showing the start of the track. Measured MSD ($\langle \Delta r2\ (t) \rangle$) as a function of delay time t for the mobile lysosome trajectories was taken at sampling rates of 1.3 s per frame on NHF cells (green circles) and Lowe 1676 cells (red circles). Data from a single cell is used in the ensemble average. Linear fitting of the MSD plot in the range from t between 20–50s region produces a diffusion coefficient for the NHF cells and Lowe 1676 cells.

Statistical analysis

All statistical analysis was performed using Graphpad7 (Prism) software. Results are expressed as mean values ± SEM. Statistical analysis was performed using unpaired *t*-test or two-way ANOVA for comparison of various treatments as indicated. A (*P*-value) of less than 0.05 was considered statistically significant.

Data availability

All data needed to evaluate the conclusions in the paper are present in the paper and/or the Expanded View. No data were deposited in a public database. Additional data related to this paper may be requested from the authors.

Expanded View for this article is available online.

Acknowledgements

We thank Dr. Michael Gaynon for thoughtful comments during the preparation of this manuscript, Dr. Robert Nussbaum for the gift of the Lowe syndrome mouse model, and Elaine Chan for assistance with data organization. This work was supported by NIH/NEI K08-EY022058 (Y.S.), R01-EY025295 (Y.S.), VA merit CX001298 (Y.S.), Ziegler Foundation for the Blind (Y.S.), Showalter Foundation (Y.S.), Children's Health Research Institute Award (Y.S.), Research for Prevention of Blindness Unrestricted grant (Stanford Ophthalmology), American Glaucoma Society (Y.S.), Lowe syndrome association (Y.S.), and Knights Templar Eye Foundation (Y.S.). P30 Vision Center grant to Stanford Ophthalmology department. Y.S. is a Laurie Kraus Lacob Faculty Scholar in Pediatric Translational Medicine. R01-EY-023295 (Y.H.) R01-EY024932 (Y.H.). NIH/NEI T32 training grant T32-EY027816 (T.J.K). NIH/NEI Kirschstein-NRSA postdoctoral fellowship F32-EY032775-01 (T.J.K). NIH [grant numbers R01-EY-032159 (Y.S.), R01-EY-028106 (Y.H.), EY031063 (Y.H.)], Glaucoma Research Foundation (CFC3) (Y.H.), BrightFocus Foundation (Y.H.), and Chan Zuckerberg Initiative Neurodegeneration Collaborative Pairs Pilot Projects (Y.H.).

Author contributions

Research plan: YS and BW; Experiments: BW; Analysis of lysosome trajectories and MSD measurement of lysosome movement: WH; Construct generation: LL; Technical support: JAA and QW; Manuscript writing and revision: YS, BW, PPP, and TJK; Critical input: YH.

Conflict of interest

The authors declare that they have no conflict of interest.

References

Abdalla E, El-Beheiry A, Dieterich K, Thevenon J, Faure J, Rendu J (2018) Lowe syndrome: a particularly severe phenotype without clinical kidney involvement. *Am J Med Genet A* 176: 460 – 464

Balla T, Varnai P (2002) Visualizing cellular phosphoinositide pools with GFP-fused protein-modules. *Sci Signal* 2002: pl3

Bärenz F, Inoue D, Yokoyama H, Tegha-Dunghu J, Freiss S, Draeger S, Mayilo D, Cado I, Merker S, Klinger M *et al* (2013) The centriolar satellite protein SSX2IP promotes centrosome maturation. *J Cell Biol* 202: 81 – 95

Bokenkamp A, Ludwig M (2016) The oculocerebrorenal syndrome of Lowe: an update. *Pediatr Nephrol* 31: 2201 – 2212

Bothwell SP, Chan E, Bernardini IM, Kuo YM, Gahl WA, Nussbaum RL (2011) Mouse model for Lowe syndrome/Dent Disease 2 renal tubulopathy. *J Am Soc Nephrol* 22: 443 – 448

Cai SL, Tee AR, Short JD, Bergeron JM, Kim J, Shen JJ, Guo RF, Johnson CL, Kiguchi K, Walker CL (2006) Activity of TSC2 is inhibited by AKT-mediated phosphorylation and membrane partitioning. *J Cell Biol* 173: 279 – 289

Caviston JP, Holzbaur EL (2006) Microtubule motors at the intersection of trafficking and transport. *Trends Cell Biol* 16: 530 – 537

Cheng Y, Kim J, Li XX, Hsueh AJ (2015) Promotion of ovarian follicle growth following mTOR activation: synergistic effects of AKT stimulators. *PLoS One* 10: e0117769

Chertkova AOMM, Postma M, van Bommel N, van der Niet S, Batenburg KL, Joosen L, Gadella TWJ, Okada Y, Goedhart J (2017) Robust and bright genetically encoded fluorescent markers for highlighting structures and compartments in mammalian cells. *bioRxiv* https://doi.org/10.1101/160374 [PREPRINT]

Cole NB, Lippincott-Schwartz J (1995) Organization of organelles and membrane traffic by microtubules. *Curr Opin Cell Biol* 7: 55 – 64

Crino PB (2011) mTOR: A pathogenic signaling pathway in developmental brain malformations. *Trends Mol Med* 17: 734 – 742

De Leo MG, Staiano L, Vicinanza M, Luciani A, Carissimo A, Mutarelli M, Di Campli A, Polishchuk E, Di Tullio G, Morra V *et al* (2016) Autophagosome-lysosome fusion triggers a lysosomal response mediated by TLR9 and controlled by OCRL. *Nat Cell Biol* 18: 839 – 850

Erdmann KS, Mao Y, McCrea HJ, Zoncu R, Lee S, Paradise S, Modregger J, Biemesderfer D, Toomre D, De Camilli P (2007) A role of the Lowe syndrome protein OCRL in early steps of the endocytic pathway. *Dev Cell* 13: 377 – 390

Fantus D, Rogers NM, Grahammer F, Huber TB, Thomson AW (2016) Roles of mTOR complexes in the kidney: implications for renal disease and transplantation. *Nat Rev Nephrol* 12: 587 – 609

Festa BP, Chen Z, Berquez M, Debaix H, Tokonami N, Prange JA, Hoek GVD, Alessio C, Raimondi A, Nevo N *et al* (2018) Impaired autophagy bridges lysosomal storage disease and epithelial dysfunction in the kidney. *Nat Commun* 9: 161

Fry AM, Mayor T, Meraldi P, Stierhof YD, Tanaka K, Nigg EA (1998) C-Nap1, a novel centrosomal coiled-coil protein and candidate substrate of the cell cycle-regulated protein kinase Nek2. *J Cell Biol* 141: 1563 – 1574

Gervais L, Claret S, Januschke J, Roth S, Guichet A (2008) PIP5K-dependent production of PIP2 sustains microtubule organization to establish polarized transport in the *Drosophila* oocyte. *Development* 135: 3829 – 3838

Gillingham AK, Munro S (2000) The PACT domain, a conserved centrosomal targeting motif in the coiled-coil proteins AKAP450 and pericentrin. *EMBO Rep* 1: 524 – 529

Hagemann N, Hou X, Goody RS, Itzen A, Erdmann KS (2012) Crystal structure of the Rab binding domain of OCRL1 in complex with Rab8 and functional implications of the OCRL1/Rab8 module for Lowe syndrome. *Small GTPases* 3: 107 – 110

He W, Song H, Su Y, Geng L, Ackerson BJ, Peng HB, Tong P (2016) Dynamic heterogeneity and non-Gaussian statistics for acetylcholine receptors on live cell membrane. *Nat Commun* 7: 11701

Hori A, Ikebe C, Tada M, Toda T (2014) Msd1/SSX2IP-dependent microtubule anchorage ensures spindle orientation and primary cilia formation. *EMBO Rep* 15: 175 – 184

Korolchuk VI, Saiki S, Lichtenberg M, Siddiqi FH, Roberts EA, Imarisio S, Jahreiss L, Sarkar S, Futter M, Menzies FM *et al* (2011) Lysosomal positioning coordinates cellular nutrient responses. *Nat Cell Biol* 13: 453 – 460

Lawrence RE, Zoncu R (2019) The lysosome as a cellular centre for signalling, metabolism and quality control. *Nat Cell Biol* 21: 133 – 142

Li X, Rydzewski N, Hider A, Zhang X, Yang J, Wang W, Gao Q, Cheng X, Xu H (2016) A molecular mechanism to regulate lysosome motility for lysosome positioning and tubulation. *Nat Cell Biol* 18: 404 – 417

Lowe M (2005) Structure and function of the Lowe syndrome protein OCRL1. *Traffic* 6: 711 – 719

Luo N, West CC, Murga-Zamalloa CA, Sun L, Anderson RM, Wells CD, Weinreb RN, Travers JB, Khanna H, Sun Y (2012) OCRL localizes to the primary cilium: a new role for cilia in Lowe syndrome. *Hum Mol Genet* 21: 3333 – 3344

Madhivanan K, Mukherjee D, Aguilar RC (2012) Lowe syndrome: between primary cilia assembly and Rac1-mediated membrane remodeling. *Commun Integr Biol* 5: 641 – 644

Matteoni R, Kreis TE (1987) Translocation and clustering of endosomes and lysosomes depends on microtubules. *J Cell Biol* 105: 1253 – 1265

McCrea HJ, Paradise S, Tomasini L, Addis M, Melis MA, De Matteis MA, De Camilli P (2008) All known patient mutations in the ASH-RhoGAP domains of OCRL affect targeting and APPL1 binding. *Biochem Biophys Res Commun* 369: 493 – 499

Nazarewicz RR, Salazar G, Patrushev N, Hilenski L, Martin AS, Xiong SQ, Ushio-Fukai M, Alexander RW (2009) Central role of early endosomal antigen 1 (EEA1) in organization of angiotensin II signaling leading to Akt activation in early endosome. *Circulation* 120: S1078

Oltrabella F, Pietka G, Ramirez IB, Mironov A, Starborg T, Drummond IA, Hinchliffe KA, Lowe M (2015) The Lowe syndrome protein OCRL1 is required for endocytosis in the zebrafish pronephric tubule. *Plos Genet* 11: e1005058

Parenti G, Andria G, Ballabio A (2015) Lysosomal storage diseases: from pathophysiology to therapy. *Annu Rev Med* 66: 471 – 486

Petry S, Vale RD (2015) Microtubule nucleation at the centrosome and beyond. *Nat Cell Biol* 17: 1089 – 1093

Ponting CP (2006) A novel domain suggests a ciliary function for ASPM, a brain size determining gene. *Bioinformatics* 22: 1031 – 1035

Sabatini DM (2017) Twenty-five years of mTOR: Uncovering the link from nutrients to growth. *Proc Natl Acad Sci USA* 114: 11818 – 11825

Saci A, Cantley LC, Carpenter CL (2011) Rac1 regulates the activity of mTORC1 and mTORC2 and controls cellular size. *Mol Cell* 42: 50 – 61

Schou KB, Morthorst SK, Christensen ST, Pedersen LB (2014) Identification of conserved, centrosome-targeting ASH domains in TRAPPII complex subunits and TRAPPC8. *Cilia* 3: 6

Ungewickell AJ, Majerus PW (1999) Increased levels of plasma lysosomal enzymes in patients with Lowe syndrome. *Proc Natl Acad Sci USA* 96: 13342 – 13344

Xu Q, Zhang Y, Wei Q, Huang Y, Hu J, Ling K (2016) Phosphatidylinositol phosphate kinase PIPKIgamma and phosphatase INPP5E coordinate initiation of ciliogenesis. *Nat Commun* 7: 10777

Zhang X, Jefferson AB, Auethavekiat V, Majerus PW (1995) The protein deficient in Lowe syndrome is a phosphatidylinositol-4,5-bisphosphate 5-phosphatase. *Proc Natl Acad Sci USA* 92: 4853 – 4856

